

ESTIMATING LUMINOSITY FUNCTION CONSTRAINTS FROM HIGH-REDSHIFT GALAXY SURVEYS

BRANT E. ROBERTSON¹

Astronomy Department, California Institute of Technology, MC 249-17, 1200 East California Boulevard, Pasadena, CA 91125

Draft version July 18, 2019

ABSTRACT

The installation of the Wide Field Camera 3 (WFC3) on the Hubble Space Telescope (HST) will revolutionize the study of high-redshift galaxy populations. Initial observations of the HST Ultra Deep Field (UDF) have yielded multiple $z \gtrsim 7$ dropout candidates. Supplemented by the Great Observatory Origins Deep Survey (GOODS) Early Release Science (ERS) and further UDF pointings, these data will provide crucial information about the most distant known galaxies. However, achieving tight constraints on the $z \sim 7$ galaxy luminosity function (LF) will require even more ambitious photometric surveys. Using a Fisher matrix approach to fully account for Poisson and cosmic sample variance, as well as covariances in the data, we estimate the uncertainties on LF parameters achieved by surveys of a given area and depth. Applying this method to WFC3 $z \sim 7$ dropout galaxy samples, we forecast the LF parameter uncertainties for a variety of model surveys. We demonstrate that performing a wide area ($\sim 1 \text{ deg}^2$) survey to $H_{\text{AB}} \sim 27$ depth or increasing the UDF depth to $H_{\text{AB}} \sim 30$ provides excellent constraints on the high- z LF when combined with the existing UDF GO and GOODS ERS data. We also show that the shape of the matter power spectrum may limit the possible gain of splitting wide area ($\gtrsim 0.5 \text{ deg}^2$) high-redshift surveys into multiple fields to probe statistically independent regions; the increased root-mean-squared density fluctuations in smaller volumes mostly offset the improved variance gained from independent samples.

Subject headings: surveys—methods: statistical—galaxies:abundances

1. INTRODUCTION

Recent studies using Hubble Space Telescope (HST) Wide Field Camera 3 (WFC3) observations have discovered tens of candidate galaxies at redshifts $z \gtrsim 7$ (Bouwens et al. 2009a,b, 2010; Oesch et al. 2010b,a; Bunker et al. 2009; McLure et al. 2009; Yan et al. 2009; Wilkins et al. 2009; Labbé et al. 2009, 2010; Finkelstein et al. 2009). The new WFC3 observations have broadened our knowledge of the highest redshift galaxies yet found, complementing $z \gtrsim 7$ galaxy searches with the Near Infrared Camera and Multi-Object Spectrometer (Kneib et al. 2004; Bouwens et al. 2004, 2005; Egami et al. 2005; Henry et al. 2007, 2008, 2009; Richard et al. 2008; Bradley et al. 2008; Bouwens et al. 2008; Zheng et al. 2009; Oesch et al. 2009; Gonzalez et al. 2009), ground-based dropout selections (Richard et al. 2006; Stanway et al. 2008; Ouchi et al. 2009a; Hickey et al. 2009; Castellano et al. 2009), and narrow band Lyman- α (Ly α) emission surveys (Parkes et al. 1994; Kodaira et al. 2003; Santos et al. 2004; Willis & Courbin 2005; Willis et al. 2008; Taniguchi et al. 2005; Stark & Ellis 2006; Iye et al. 2006; Kashikawa et al. 2006; Stark et al. 2007a; Cuby et al. 2007; Ota et al. 2008; Ouchi et al. 2009b; Hibon et al. 2009; Sobral et al. 2009). The existence of star-forming galaxies at $z \gtrsim 7$ has been well-established by these studies, and the importance of these high redshift galaxies for reionization and

obtain requires an estimate of the uncertainty in the abundance of galaxies as a function of luminosity. In addition to the Poisson uncertainty inherent in galaxy counts, cosmic sample variance induced by density fluctuations and galaxy clustering must be accounted for (see, e.g., Newman & Davis 2002; Somerville et al. 2004; Stark et al. 2007b). A particularly powerful approach for estimating these uncertainties and determining the resulting potential constraints on the luminosity function of galaxies in the UDF was presented by Trenti & Stiavelli (2008). These authors used cosmological simulations to determine the abundance and spatial distribution of dark matter halos and then applied a model for the halo mass-to-light ratio to determine the abundance of galaxies of a given luminosity. Poisson and sample variance uncertainties were estimated by drawing pencil beam realizations of the survey from the cosmological volume (see also Kitzbichler & White 2007). A maximum-likelihood approach was then used to study constraints on the luminosity function for various dropout selections.

The maximum-likelihood estimation of LF parameters based on mock catalogues can account for detailed selection effects and spatial correlations in addition to the Poisson and sample variance uncertainties. Such simulations have clear advantages for estimating the completeness of magnitude-limited surveys or understanding systematic effects intro-

$200h^{-1}\text{Mpc}$) cosmological simulations are required to probe multiple independent samples of the surveys' high-redshift galaxy populations. For instance, a $\sim 1 \text{ deg}^2$ survey at $6.5 \lesssim z \lesssim 7.5$ has a comoving volume of $V \approx 3 \times 10^6 h^{-3} \text{Mpc}^3$. The largest simulation used by Trenti & Stiavelli (2008) would provide less than two independent samples of such a volume, and even the Millennium Simulation (Springel et al. 2005) with a comoving box size $L = 500h^{-1}\text{Mpc}$ would only provide ~ 40 independent samples of such a wide high-redshift survey. Second, the method requires access to and manipulation of cosmological simulation results. This requirement may pose an unwanted computational overhead for those interested in rapid estimates and comparisons of potential constraints from a wide range of survey designs.

A simpler methodology for estimating survey constraints on the abundance of high-redshift galaxies that does not directly require halo catalogues from cosmological simulations is therefore desirable for performing rapid comparisons of survey designs. Hence, we seek an approximate method for forecasting LF parameter constraints that relies on descriptions of galaxy and dark matter halo abundance and clustering, Poisson and cosmic sample variance, and parameter covariances that are analytical or easily calculable through numerical methods. We utilize a simple model for describing the clustering of $z \sim 7$ galaxies based on fiducial empirical estimates of the high-redshift galaxy luminosity function (Oesch et al. 2010b) and abundance matching between galaxies and dark matter halos (e.g., Conroy et al. 2006; Conroy & Wechsler 2009). We then adopt a common approach to translate galaxy clustering and matter fluctuations into an estimate of the cosmic sample variance (see the various calculations in, e.g., Newman & Davis 2002; Somerville et al. 2004; Stark et al. 2007b; Trenti & Stiavelli 2008). With this estimate of the sample variance and Poisson uncertainty from an assumed fiducial model for the abundance of galaxies, we use a Fisher matrix formalism to characterize the likelihood function and estimate $z \sim 7$ luminosity function parameter constraints. The presented methodology is fast and flexible, and can be used with appropriate extensions, to estimate constraints on galaxy abundance for other survey sample selections and redshifts.

Motivated by the exciting recent HST WFC3 results, we focus on modeling $z \sim 7$ dropout survey designs. While we choose to study broadband searches for high-redshift galaxies, narrow band surveys for high-redshift Ly α emission present another interesting class of survey designs. The rapid progress in detecting increasing numbers of high-redshift Ly α emitters using narrow band surveys has motivated theoretical efforts both to understand and predict the abundance of Ly α emitters. The observable properties of the high-redshift Ly α emitter population are particularly difficult to model owing to the uncertain escape fraction, intergalactic medium absorption and other radiative transfer effects, as well as uncertainties in

amine the statistical constraining power of various broadband survey designs and will not attempt to model the Ly α emitter population.

This paper is organized as follows. Forecasting constraints on $z \sim 7$ LF function parameters requires a model of the sources of error and covariances in the data. In §2, we discuss sample variance uncertainties owing to cosmic density fluctuations. In §3, we review the Fisher matrix formalism and show how to apply the formalism to forecast LF parameter uncertainties accounting for cosmic sample and Poisson variances. To perform actual forecasts for the $z \sim 7$ LF, we review existing HST WFC3 survey data in §5 and define fiducial model surveys in §6. In §7, we combine the expected constraints from existing surveys with forecasts of luminosity function constraints from model surveys. We discuss our results and possible caveats in §8, and summarize and conclude in §9.

Throughout, we work in the context of a ΛCDM cosmology consistent with joint constraints from the 5-year Wilkinson Microwave Anisotropy Probe, Type Ia supernovae, Baryon Acoustic Oscillation, and Hubble Key Project data (Freedman et al. 2001; Percival et al. 2007; Kowalski et al. 2008). Specifically, we adopt a Hubble parameter $h = 0.705$, matter density $\Omega_m = 0.274$, dark energy density $\Omega_\Lambda = 0.726$, baryon density $\Omega_b = 0.0456$, relativistic species density $\Omega_r = 4.15 \times 10^{-5}$, spectral index $n_s = 0.96$, and root-mean-squared density fluctuations in $8 h^{-1}\text{Mpc}$ -radius spheres of $\sigma_8 = 0.812$ (Komatsu et al. 2009). We report all magnitudes in the AB system (Oke & Gunn 1983).

2. POISSON UNCERTAINTY, COSMIC SAMPLE VARIANCE, AND THE ΛCDM POWER SPECTRUM

We wish to evaluate the relative merits of various galaxy survey designs in terms of their ability to constrain the galaxy luminosity function. To perform this evaluation, we must determine the quality of each design in terms of the number of galaxies of a given luminosity the survey will discover (the Poisson variance) and the intrinsic scatter expected for the survey volume given variations in the cosmological density field (the cosmic sample variance). This section of the paper formally defines each source of uncertainty and describes how these variances are calculated.

We define cosmic sample variance as the fluctuations in a volume-averaged quantity owing to density inhomogeneities seeded by the matter power spectrum. We will use the terms “cosmic variance” and “sample variance” interchangeably, but elsewhere in the literature cosmic variance is taken to equal the sample variance only in the limit of the entire volume of the universe (e.g., Hu & Kravtsov 2003).

2.1. Dark Matter Density Variance

Density fluctuations, or differences between the local matter density $\rho_m(\mathbf{x})$ and the mean matter density $\bar{\rho}_m$, can be described in terms of a local matter overdensity $\delta(\mathbf{x}) \equiv [\rho_m(\mathbf{x}) - \bar{\rho}_m] / \bar{\rho}_m$. Consider a survey of comoving volume V at redshift

a dependence on the direction of the wavenumber \mathbf{k} , $D(z)$ is the linear growth function, and $P(k)$ is the isotropic linear Λ CDM power spectrum. To calculate $P(k)$, we use the transfer function of Eisenstein & Hu (1998) that includes the effects of baryons. We ignore possible nonlinear corrections to the power spectrum (e.g., Peacock & Dodds 1996; Smith et al. 2003). The window function is normalized such that $\int d^3x W(\mathbf{x}) = 1$. For a spherical volume of comoving radius $R = 8h^{-1}\text{Mpc}$, Equation 1 would provide $\sigma_{\text{DM}} = \sigma_8$ at redshift $z = 0$. The linear growth function

$$D(z) = D_0 H(z) \int_z^\infty \frac{(1+z') dz'}{H^3(z')} \quad (2)$$

has a normalization constant D_0 chosen such that $D(z=0) = 1$. The Hubble parameter

$$H(z) = H_0 [\Omega_r (1+z)^4 + \Omega_m (1+z)^3 + (1 - \Omega_m - \Omega_\Lambda - \Omega_r) (1+z)^2 + \Omega_\Lambda]^{1/2} \quad (3)$$

describes the rate of change of the universal scale factor $H \equiv \dot{a}/a$ as a function of the matter density Ω_m , relativistic species density Ω_r , and dark energy density Ω_Λ (taken to be a cosmological constant).

2.2. Dark Matter Halo Abundance and Clustering

For galaxy surveys, where quantities of interest depend on the abundance and clustering of galaxies, the sample variance will depend on the bias of dark matter halos hosting the observed systems. We can define the bias in terms of the correlation function as $b^2 = \xi_h/\xi_m$ where ξ_h is the correlation function of dark matter halos. Given a halo mass function, the bias of halos with mass m can be estimated using the peak-background split formalism (e.g., Kaiser 1984; Mo & White 1996; Sheth & Tormen 1999) or measured directly from the simulations via the halo correlation function or halo power spectrum. We adopt the latter approach.

We use the dark matter halo mass function measured by Tinker et al. (2008) from a large suite of cosmological simulations (Kravtsov et al. 2004; Warren et al. 2006; Crocce et al. 2006; Gottlöber & Yepes 2007; Yepes et al. 2007). The Tinker et al. (2008) mass function can be written as a function of the dark matter halo mass m in terms of the ‘‘peak height’’,

$$\nu = \frac{\delta_c}{D(z)\sigma(m)}, \quad (4)$$

where $\delta_c = 1.686$ is the spherical collapse barrier (see, e.g., Gunn & Gott 1972; Bond & Myers 1996), $D(z)\sigma(m)$ is the square root of the dark matter variance (Equation 1) evaluated in a spherical volume of comoving radius $R = (3m/4\pi\bar{\rho}_m)^{1/3}$. Here, $\bar{\rho}_m$ is the background matter density. The linear growth function $D(z)$ is given by Equation 2.

With the definition of peak height ν in Equation 4, the

simulated mass function measured for halos defined with a spherical overdensity $\Delta = 200$ relative to the background matter density (see also §4 of Tinker et al. 2010). The abundance of dark matter halos more massive than m is then just $n_h(> m) = \int_m^\infty (dn_h/dm) dm$.

We choose the Tinker et al. (2008) mass function because it is accurate to $\lesssim 5\%$ for halos in the mass range $10^{11} h^{-1} M_\odot \leq m \leq 10^{15} h^{-1} M_\odot$ at redshift $z = 0$, and improves on previous approximations by 10–20% (c.f., Sheth & Tormen 1999). Tinker et al. (2008) demonstrate that the halo mass function does not have a redshift-independent, universal form, and that the normalization of the first crossing distribution evolves at the 20–50% level between $z = 0$ and $z = 2.5$. However, the halo mass function has not been calibrated at the redshifts of interest ($z \gg 2.5$) and following the advice in §4 of Tinker et al. (2008) we will use the $z = 2.5$ mass function as the best available approximation. We note that using any other previously published mass function from the literature (e.g., Sheth & Tormen 1999) will therefore introduce an unknown error in the abundance of halos at high redshifts. Tinker et al. (2008) estimate this error could be as large as $\sim 20\text{--}50\%$ for galaxy-sized halos.

For the bias b relating halo and dark matter clustering, we will use the results of Tinker et al. (2010) who measure the halo bias as a function of peak height ν in a manner consistent with the halo mass function of Tinker et al. (2008). The bias function $b(\nu)$ is constrained by the halo first crossing distribution $f(\nu)$ by requiring that dark matter is not biased against itself, i.e.,

$$\int b(\nu) f(\nu) d\nu = 1. \quad (7)$$

Under this constraint, Tinker et al. (2010) find that the fitting function

$$b(\nu) = 1 - A \frac{\nu^a}{\nu^a + \delta_c^a} + B\nu^b + C\nu^c \quad (8)$$

with parameters $A = 1.0$, $a = 0.1325$, $B = 0.183$, $b = 1.5$, $C = 0.265$, and $c = 2.4$ provides an accurate match to the bias of dark matter halos defined with a spherical overdensity of $\Delta = 200$ relative to the background matter density. As demonstrated by Tinker et al. (2010), Equation 8 reproduces the simulated halo clustering better than the analytical formulae of Mo & White (1996) or Sheth et al. (2001) calculated using the peak-background split formalism. Tinker et al. (2010) find that the bias $b(\nu)$ as a function of peak height ν is nearly redshift-independent, and we will adopt Equation 8 for $b(\nu)$ at all redshifts.

2.3. Galaxy Abundance and Clustering

Our main premise is to use the Fisher matrix approach to estimate the constraints on a model for the abundance of galaxies that reproduces well the observed source counts. The def-

lower redshifts, additional constraints on the connection between galaxy and halo populations are attainable (see, e.g., Lee et al. 2009).

We will adopt the commonly-used Schechter (1976) model for the abundance of galaxies. Specifically, the expected number density \bar{n}_i of galaxies in the i -th luminosity bin of width ΔM about magnitude M_i can be written

$$\bar{n}_i = \int_{M_i - \Delta M/2}^{M_i + \Delta M/2} \Phi(M) dM, \quad (9)$$

where the Schechter (1976) function

$$\Phi(M) = \frac{2}{5} \ln(10) \phi_* \left[10^{\frac{2}{5}(M_* - M)} \right]^{\alpha+1} \exp \left[-10^{\frac{2}{5}(M_* - M)} \right], \quad (10)$$

describes the distribution of galaxy luminosities, ϕ_* is the luminosity function normalization in comoving $\text{Mpc}^{-3} \text{mag}^{-1}$, M_* is the characteristic galaxy luminosity in AB magnitudes, and α is the faint-end slope. We will often refer to the parameters of this Schechter (1976) model in terms of the vector $\mathbf{p} = [\log_{10} \phi_*, M_*, \alpha]$, and it is these parameters for which we will forecast constraints. The fiducial values for the parameters \mathbf{p} used in the Fisher matrix calculation will be selected in §5.

In a manner similar to Equation 9, we can also define the comoving abundance \bar{n}_L of galaxies more luminous than magnitude M as $\bar{n}_L(< M) = \int_{-\infty}^M \Phi(M) dM$, where the negative lower limit follows from the definition of magnitudes.

With a model for the abundance of galaxies, we will associate galaxies with dark matter halos of similar abundance to estimate the galaxies' spatial clustering. The abundance \bar{n}_i of galaxies in the range $M_i \pm \Delta M/2$ can be written as $\bar{n}_i \equiv \bar{n}_L(< M_i + \Delta M/2) - \bar{n}_L(< M_i - \Delta M/2)$. We match the abundance of galaxies and halos as

$$n_h(> m) \simeq \bar{n}_L(< M) \quad (11)$$

at the minimum and maximum luminosity of galaxies in each magnitude bin (e.g., $M = M_i + \Delta M/2$ and $M = M_i - \Delta M/2$), which provides a mass range $m_i \pm \Delta m/2$ of halos with a similar abundance (e.g., Conroy et al. 2006; Conroy & Wechsler 2009). The comoving number density of these halos is simply $n_{h,i} \equiv n_h(> m_i - \Delta m/2) - n_h(> m_i + \Delta m/2)$, with $n_{h,i} = \bar{n}_i$. The resulting connection between galaxy luminosity and halo mass is simplistic, but more sophisticated stellar mass-halo mass relations could be incorporated into our approach when warranted by the constraining power of the available data (see, e.g., Behroozi et al. 2010). We adopt $\Delta M = 0.25$ mag throughout, but we have checked that our conclusions also hold for $\Delta M = 0.5$ or $\Delta M = 0.1$.

The bias b_i of galaxies in the range $M_i \pm \Delta M/2$ is then approximated as the number-weighted average clustering of halos of mass $m_i \pm \Delta m/2$. We can express b_i as

scales, the actual measured number density of galaxies in the magnitude range $M \pm \Delta M/2$ at location \mathbf{x} will be

$$n_i(\mathbf{x}, z) = \bar{n}_i [1 + b_i \delta(\mathbf{x}, z)] \quad (13)$$

where $\delta(\mathbf{x}, z)$ is the local linear overdensity and the bias b_i is determined in Equation 12. The large scale structure of the matter density field will cause the galaxy counts to covary. The sample covariance S_{ij} between galaxies in the i -th and j -th magnitude bins is simply the average squared difference between the measured galaxy density n and the expected average galaxy density \bar{n} for each bin. We can then write the sample covariance as

$$S_{ij} \equiv \langle (n_i - \bar{n}_i)(n_j - \bar{n}_j) \rangle, \quad (14)$$

where the average is taken over all N_{fields} fields of the survey. Given Equations 1, 8, 9, 12, and 13, we can evaluate the elements of the sample covariance matrix \mathbf{S} as

$$S_{ij} = \frac{b_i b_j \bar{n}_i \bar{n}_j}{N_{\text{fields}}} \int \frac{d^3 k}{(2\pi)^3} \hat{W}_i(\mathbf{k}) \hat{W}_j^*(\mathbf{k}) P(k) \quad (15)$$

where $\hat{W}_i(\mathbf{k})$ is the k -space window function for the survey field volume of the i -th magnitude bin. Depending on, e.g., the redshift distribution of sources with different magnitudes, or some luminosity-dependent completeness, we could have $\hat{W}_i(\mathbf{k}) \neq \hat{W}_j(\mathbf{k})$ in general. However, throughout the rest of the paper we will consider only galaxy densities and variances within the entire effective survey volume, such that the elements of the sample covariance matrix \mathbf{S} refer to luminosity bins within the same volume of each field. We will therefore write $\hat{W}_i(\mathbf{k}) \hat{W}_j^*(\mathbf{k}) = |\hat{W}_V(\mathbf{k})|^2$, where

$$\hat{W}_V(\mathbf{k}) = \text{sinc} \left(\frac{k_x r \Theta_x}{2} \right) \text{sinc} \left(\frac{k_y r \Theta_y}{2} \right) \text{sinc} \left(\frac{k_z \delta r}{2} \right) \quad (16)$$

is an approximate k -space window function for the effective volume V of a survey at comoving radial distance r , comoving radial width δr , and rectangular area $\Theta_x \times \Theta_y$ in square radians.² The function $\text{sinc}(x/2) = 2 \sin(x/2)/x$ is the Fourier transform of the Heaviside $\Pi(x)$ unit box. Similar window functions were adopted by Newman & Davis (2002) and Stark et al. (2007b) in their estimates of cosmic variance.

Unless otherwise specified, when discussing the cosmic sample variance uncertainty or error we will refer to the averaged quantity

$$\sigma_{\text{CV}} \equiv \langle b \rangle D(z) \sigma_{\text{DM}} / \sqrt{N_{\text{fields}}}, \quad (17)$$

where $\langle b \rangle$ is the average bias of all galaxies in a survey field. This quantity σ_{CV} is the cosmic variance uncertainty that is often reported for surveys, but is distinct from the elements sample covariance matrix S_{ij} since the latter involves the bias of galaxies in individual luminosity bins.

ΛCDM power spectrum through the survey volume and geometry. For a fixed amount of observing time, splitting a survey into $N_{\text{fields}} = 2$ fields will rescale the volume of each field by $V \propto 1/N_{\text{fields}}$ and result in a corresponding increase in the typical dark matter density fluctuations in each field. For very large surveys, the decrease in the volume per field can (at least partially) offset the gains achieved by probing multiple independent samples.

The left panel of Figure 1 shows the RMS density fluctuations $D(z)\sigma_{\text{DM}}/\sqrt{N_{\text{fields}}}$ in a survey at redshifts $6.5 \leq z \leq 7.5$ as a function of total area for multiple fields ($N_{\text{fields}} = 1, 2, 4$). For a galaxy survey, the sample variance in each luminosity bin will be increased by a factor of the galaxy bias (see Equation 15). While the uncertainty from RMS density fluctuations will improve with the addition of statistically-independent samples, the fractional improvement is less than $1 - 1/\sqrt{N_{\text{fields}}}$ for large volumes. The right panel of Figure 1 shows the fractional improvement gained by multiple fields. For a flat power spectrum, the improvement would be $1 - 1/\sqrt{2} = 0.293$ for $N_{\text{fields}} = 2$ and $1 - 1/\sqrt{4} = 0.5$ for $N_{\text{fields}} = 4$.

2.5. Poisson Variance from Galaxy Abundance

Number-counting statistics will naturally introduce a Poisson variance into the galaxy number count statistics. The diagonal Poisson variance matrix \mathbf{P} will only add to the total covariance for counts within a single magnitude bin (i.e., only when $i = j$). For definiteness, we will express the Poisson covariance as

$$P_{ij} = \frac{\delta_{ij}\bar{n}_i}{V_i} \quad (18)$$

where the Kronecker $\delta_{ij} = 1$ for $i = j$ and $\delta_{ij} = 0$ for $i \neq j$.

3. PARAMETER ESTIMATION AND THE FISHER MATRIX

Fisher (1935) illustrated how to infer inductively the properties of statistical populations from data samples. By approximating the likelihood function as a Gaussian near its maximum and assuming a parameterized model, the uncertainties in the model parameters allowed by a future data set can be estimated directly from the data covariances. Interested readers should refer to the excellent and detailed discussion of the Fisher matrix formalism provided in §2 of Tegmark et al. (1997), but we outline the general approach below.

We aim to estimate the uncertainties on model parameters p_μ (the “parameter covariance matrix” \mathbf{C}) achieved by the data produced by some fiducial survey. The quality of the future data for each fiducial survey will be characterized by the “data covariance matrix” \mathbf{D} . The elements D_{ij} of the total data covariance matrix are simply the sum of the sample covariance and Poisson uncertainties described in §2.4 and §2.5, which we can write as

$$D_{ij} = S_{ij} + P_{ij}, \quad (19)$$

2009; Wu et al. 2009, and especially the discussion in §III of Lima & Hu 2004). Here, $\text{Tr}(\mathbf{A}) = \sum_{i=1}^m A_{ii}$ for an $m \times m$ matrix. The vector elements p_μ reflect the parameters of the data model \bar{n} . The first term of Equation 20 models second derivatives of the likelihood function in the Poisson error-dominated regime (Holder et al. 2001), while the second term models the sample covariance-dominated regime (Tegmark et al. 1997, see also Appendix A of Vogeley & Szalay 1996). The derivatives $\partial\bar{n}/\partial p_\mu$ of the luminosity function model are computed directly by differentiating Equation 9. The derivatives $\partial\mathbf{S}/\partial p_\mu$ of the sample covariance matrix are evaluated numerically since changes to the model luminosity function alter the galaxy bias b in Equation 15 for a given luminosity bin in a nontrivial way.

Once the Fisher matrix \mathbf{F} is calculated, estimating the parameter covariance matrix \mathbf{C} becomes straightforward. The elements of the parameter covariance matrix are approximated as

$$C_{\mu\nu} \approx (\mathbf{F}^{-1})_{\mu\nu}. \quad (21)$$

The marginalized uncertainty on parameter p_μ is then

$$\sigma_\mu \equiv C_{\mu\mu}^{1/2} = (\mathbf{F}^{-1})_{\mu\mu}^{1/2}. \quad (22)$$

Similarly, we can estimate the unmarginalized error on each parameter as $\sigma_\mu^u = F_{\mu\mu}^{-1/2}$. However, in what follows when we discuss the “error” or “uncertainty” on luminosity function parameters we mean the marginalized error unless otherwise stated.

We will apply the above formalism to estimate the relative constraining power of possible galaxy surveys, but we will focus on evaluating such surveys in the context of existing and forthcoming data from observational programs already underway (i.e., the WFC3 UDF GO and GOODS ERS data). Our statistical formalism provides a simple way to incorporate constraints from prior data. The combined constraints $\mathbf{C}_{\text{combo}}$ of a prior observation $\mathbf{C}_{\text{prior}}$ supplemented by the forecasted constraints of a future survey \mathbf{C} can be estimated as

$$\mathbf{C}_{\text{combo}} = (\mathbf{C}^{-1} + \mathbf{C}_{\text{prior}}^{-1})^{-1}, \quad (23)$$

or, in other words, the combined parameter covariance matrix is the inverse of the sum of the Fisher matrices of the prior and future surveys. Depending on the magnitude of the off diagonal elements of \mathbf{C} and $\mathbf{C}_{\text{prior}}$, the combined parameter covariance matrix $\mathbf{C}_{\text{combo}}$ can provide a substantially different correlation between parameters than either the prior or future surveys produce individually. As a result, the marginalized uncertainty on parameters can benefit substantially by combining surveys with different characteristics. These ramifications of Equation 23 will become more apparent in §7.

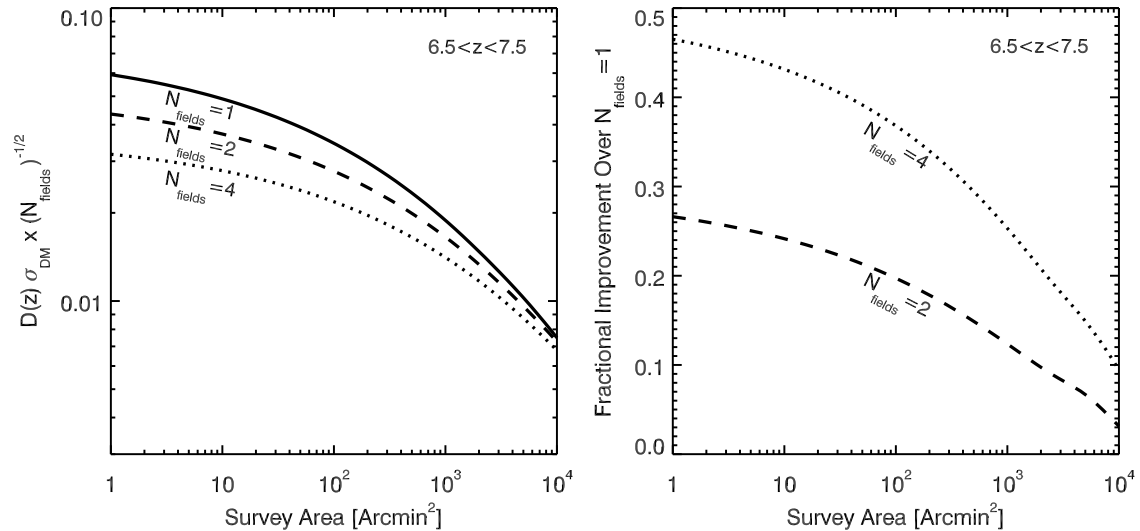


FIG. 1.— Root-mean-squared (RMS) density fluctuations in a survey at redshift $6.5 \leq z \leq 7.5$ as a function of total area (right panel). Uncertainties owing to RMS density fluctuations scale with the product of the growth function $D(z)$ and the $z = 0$ RMS dark matter fluctuations σ_{DM} . If the Λ CDM power spectrum σ_{DM} for the rectangular survey geometry was flat, multiple field surveys would improve their combined RMS density fluctuations by $1/\sqrt{N_{\text{fields}}}$ if they probed widely-separated, statistically-independent regions. However, the shape of the Λ CDM power spectrum σ_{DM} limits this improvement since the multiple fields each probe a volume V/N_{fields} and the power increases toward small scales. Shown are the RMS density fluctuations for multiple field surveys ($N_{\text{fields}} = 1$, solid line; $N_{\text{fields}} = 2$, dashed line; $N_{\text{fields}} = 4$, dotted line). The left panel shows the fractional improvement in uncertainties owing to density fluctuations gained by splitting survey into $N_{\text{fields}} = 2$ (dashed line) or $N_{\text{fields}} = 4$ smaller fields of equivalent total area. If σ_{DM} were independent of scale, the fractional improvement would be a constant $1 - 1/\sqrt{2} = 0.293$ for $N_{\text{fields}} = 2$ and $1 - 1/\sqrt{4} = 0.5$ for $N_{\text{fields}} = 4$.

ance by altering the halo-galaxy correspondence in Equation 11.

Of these survey characteristics, we will keep z_{min} , z_{max} , f_{comp} , and f_{occ} fixed between surveys. We will assume that the surveys are effectively volume-limited ($f_{\text{comp}} = 1$) over the redshift range of interest. Given a complete volume-limited survey, the choice of minimum and maximum redshifts roughly corresponds to the filter choice defining a dropout selection. We will adopt $z_{\text{min}} = 6.5$ and $z_{\text{max}} = 7.5$, which roughly approximates the redshift selection of the (z_{850} - Y_{105}) vs. (Y_{105} - J_{125}) color selection of Oesch et al. (2010b, see their Fig. 1). Similar selections can be defined for I_{814} -dropouts. Our calculations can be easily extended to different redshift selections, but we adopt this redshift range since the fiducial abundance of $z \sim 7$ WFC3 UDF GO galaxy candidates appears increasingly robust (see, e.g., the discussion in §2 of McLure et al. 2009), the characteristic ultraviolet (UV) luminosity of galaxies is decreasing with redshift (e.g., Bouwens et al. 2008), and the abundance of dark matter halos hosting galaxies is rapidly declining at earlier epochs.

Our model surveys will consist of WFC3 H -band coverage with equal coverage in an additional, bluer WFC3 filter. The existing and ongoing UDF GO and GOODS ERS surveys will use the $F160W$ band (see §5 below), but using the $F140W$ band buys $\approx 0.3 - 0.5$ magnitudes in sensitivity for the same exposure time, depending on the source luminosity (see below).

TABLE 1
OPTIMUM 5- σ POINT SOURCE SENSITIVITY
VS. EXPOSURE TIME PER POINTING

N_{orbits}	H_{140} [AB Mag.]	H_{160} [AB Mag.]
0.5	27.00	26.62
1.0	27.43	27.07
2.0	27.84	27.49
3.0	28.07	27.73
4.0	28.23	27.89
6.0	28.46	28.12
8.0	28.62	28.28
19.0	29.10	28.76
38.0	29.47	29.14
125.0	30.12	29.78

in this conversion (e.g., ± 0.4 magnitudes in M_{UV}).

Lastly, HST observations are conducted using some number N_{orbits} per pointing that effectively determines M_{max} . During each orbit the field visibility depends on the field declination, and the available on-source integration time also depends on observatory and instrument overheads such as guide star acquisition, filter changes, dithering, and readout. The UDF GO and GOODS ERS surveys are at a declination of $\delta \approx -27$ deg, and for ease of comparison we will assume all future surveys have $|\delta| < 30$ deg. This roughly equatorial declination range provides a visibility of 54 minutes/orbit³.

5. EXISTING SURVEYS

The discussion in §2 makes clear that the combination of different survey designs can potentially provide increased constraints beyond that achieved by individual data sets. Even duplicate surveys will reduce the Poisson variance and potentially the sample variance (especially if the fields are widely separated on the sky). In the absence of significant systematic biases, using prior data will generally improve the expected parameter uncertainty obtained by future experiments. We will therefore rely on the expected constraints achieved by the ongoing WFC3 UDF GO and GOODS ERS programs to augment the fiducial survey designs evaluated in §6 and §7. In this section, we will calculate the expected constraints provided by the UDF GO and GOODS ERS data.

Table 2 describes the field geometry, number of fields N_{fields} , total area, and expected H -band $5-\sigma$ point source depth for the UDF GO and GOODS ERS survey designs. Numerous analyses of the initial UDF GO data release have already been performed (e.g., Bouwens et al. 2009b; Oesch et al. 2010b,a; McLure et al. 2009; Bunker et al. 2009; McLure et al. 2009; Yan et al. 2009; Finkelstein et al. 2009), but we will consider the expected constraints provided by the entire 192 orbit program. The GOODS ERS data has not yet been released (but for initial analyses on unreleased ERS data see Wilkins et al. 2009; Labbé et al. 2009), and we will also use the Fisher matrix approach to estimate the constraints provided by that survey.

The UDF GO observations use the F160W filter with 19 orbits in each of two WFC3 pointings. Using the WFC3 ETC, we estimate these observations will reach $H_{\text{AB}} \approx 28.76$. The UDF GO observations also will have 38 F160W orbits in the HUDF that will reach $H_{\text{AB}} \approx 29.14^5$. The remaining 116 orbits in the program will be used for observing in bluer filters.

The GOODS ERS survey will have 3-orbit depth in F160W, using 24 orbits (out of a total 104) for H -band observations. We estimate that these observations will reach a sensitivity of $H_{\text{AB}} \approx 27.73^6$. The remaining 80 orbits in the program will be used for observations with other filters and grisms.

5.1. Forecasted Constraints for Existing Surveys

The forecasted constraints achieved by the UDF GO and GOODS ERS surveys are plotted in Figure 2. Each panel shows the constraints for the UDF GO (blue region) and GOODS ERS (light blue region) surveys separately, and in combination (dark blue region). The constraints are plotted for the $M_\star-\phi_\star$ (left panel), $M_\star-\alpha$ (middle panel), and $\phi_\star-\alpha$ (right panel) projections. In Figure 2 (and in similar figures throughout the paper), the shaded regions correspond to standard Gaussian contours.

Figure 2 highlights some general properties of the performance of different kinds of surveys for providing luminosity function parameter constraints, as well as specific features of the UDF GO and GOODS ERS surveys:

defined as

$$\rho = \frac{C_{xy}}{\sigma_x \sigma_y}, \quad (24)$$

the forecasts calculate typical correlation coefficients of $\rho \gtrsim 0.9$. For a given M_\star a narrow range of $\log_{10} \phi_\star$ or α are permitted by the data, even as the marginalized uncertainties can be as large as $\sim 30-40\%$ fractionally for $\log_{10} \phi_\star$ and α .

- The orientation of the constraint ellipse forecasted for each survey can differ significantly depending on the parameter uncertainties, even if the parameter correlation coefficients for the separate surveys are similar. The orientation of the constraint ellipse major axis with respect to the x -axis in the x - y parameter plane can be characterized by the angle

$$\Theta \equiv \frac{1}{2} \arctan \left[\frac{2\rho\sigma_x\sigma_y}{\sigma_x^2 - \sigma_y^2} \right] = \frac{1}{2} \arctan \left[\frac{2C_{xy}}{C_{xx} - C_{yy}} \right], \quad (25)$$

which depends on the correlation ρ and the parameter uncertainties. If the angle Θ differs between separate surveys, then the constraints achieved by combining the surveys can improve dramatically.

For reference, the calculated marginalized and unmarginalized errors for \mathbf{p} as well as the Pearson's correlation coefficient ρ and the angle Θ for each pair of parameters are listed for the existing surveys in Table 4.

As Figure 2 and Table 4 show, the UDF GO and GOODS ERS surveys will already provide interesting constraints on the abundance of $z \sim 7$ galaxies. When combined, the unmarginalized uncertainties on the LF parameters will be $\Delta M_\star \sim 0.1$ mag, $\Delta \log_{10} \phi_\star \lesssim 0.1$, and $\Delta \alpha \sim 0.15$. For the full UDF GO survey, we find that the unmarginalized uncertainty for the faint-end slope is $\Delta \alpha \sim 0.16$. Using a single UDF GO field and a limiting depth of $F160W \sim 29$ AB for a single pointing, Oesch et al. (2010b) report a faint-end slope uncertainty of $\Delta \alpha \sim 0.33$ when ϕ_\star and M_\star are fixed (i.e., the unmarginalized uncertainty on α). If we use the same single pointing area and depth, and the same cosmology, our estimate of the unmarginalized uncertainty would increase to $\Delta \alpha \sim 0.26$. The GOODS ERS and UDF GO surveys are complementary in that the depth of the UDF GO survey provides a beneficial constraint on the faint-end slope α . This UDF GO constraint on α rotates the UDF GO error ellipse relative to the GOODS ERS constraint in the $M_\star-\alpha$ and $\phi_\star-\alpha$ projections, thereby reducing the corresponding parameter uncertainties. Individually, the GOODS ERS uncertainties will be considerably larger than those obtained by the UDF GO survey, since the GOODS ERS survey lacks sufficient depth to tightly constrain the LF faint-end slope and is not wide enough to tightly constrain M_\star or ϕ_\star .

TABLE 2
EXISTING SURVEYS

Survey Name	Field Geometry [Arcmin. \times Arcmin.]	N_{fields} [#]	Total Area [Sq. Arcmin.]	N_{orbits} ^a [#]	H -band Depth [AB Mag.]	Ref.
UDF GO	$2.05' \times 2.27'$	2	9.3	19	28.76	1
	$2.05' \times 2.27'$	1	4.7	38	29.14	
GOODS ERS	$5.2' \times 10.3'$ ^b	1	53.3	3	27.73 ^c	2

REFERENCES. — (1) <http://www.stsci.edu/observing/phase2-public/11563.pdf>; (2) <http://www.stsci.edu/hst/proposing/old-proposing-files/goods-cdfs.pdf>

^a Number of orbits per pointing.

^b The GOODS ERS survey is a 2×4 WFC3 IR mosaic dithered to match the Ultraviolet/Visible channel field of view.

^c For details, see the discussion in §5.

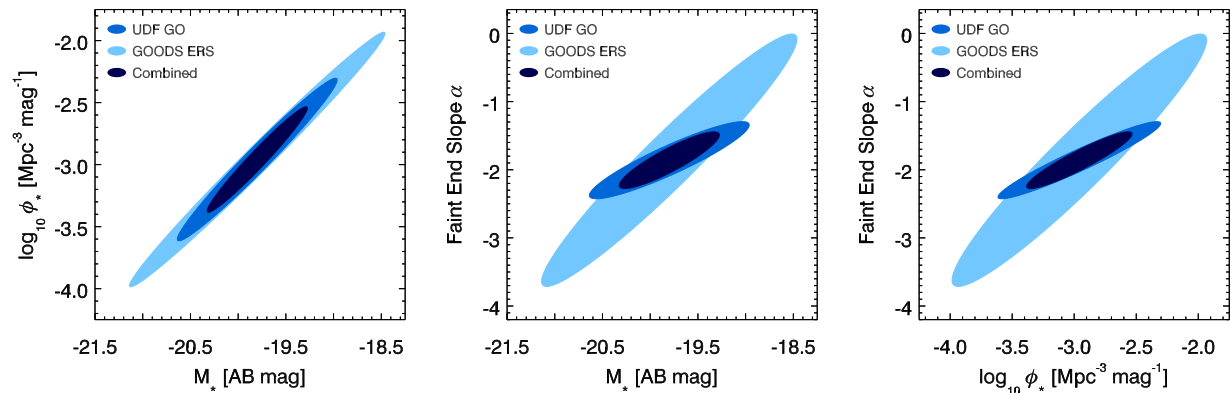


FIG. 2.— Forecasted constraints on $z \sim 7$ luminosity function parameters expected from the forthcoming UDF GO and GOODS ERS WFC3 data. The constraints are calculated for a Schechter (1976) luminosity function with a characteristic luminosity M_* , normalization ϕ_* , and faint-end slope α . Shown are the $1-\sigma$ constraints in the $M_* - \log_{10} \phi_*$ (left panel), $M_* - \alpha$ (middle panel), and $\log_{10} \phi_* - \alpha$ (right panel) space projections for the UDF GO (blue region) and GOODS ERS (light blue region) surveys. Also shown are the constraints expected by combining both surveys (dark blue region). The depth of the UDF GO survey will provide a better constraint on the faint-end slope than GOODS ERS, but the differences between their parameter covariances make them complementary.

parameter uncertainties of approximately $\Delta M_* \sim 0.2$ mag, $\Delta \phi_* \sim 0.2$, and $\Delta \alpha \sim 0.2$ depending on their covariances. To reach such constraints, these UDF GO and GOODS ERS surveys would need to be complemented by either wider area or deeper surveys. We now consider some fiducial model surveys that could achieve these constraints in combination with the UDF GO and GOODS ERS data.

6. MODEL SURVEYS

The complete UDF GO and GOODS ERS surveys will provide extremely interesting initial data on the abundance of $z \sim 7$ galaxies, but the marginalized uncertainties on the LF parameters achieved by those surveys will still permit uncertainties of $\sim 25\%$ in the total number of galaxies at $M_{\text{UV}} \lesssim -18$. We can repeat the calculations from §5 for fiducial model surveys to illustrate what constraints wider or deeper surveys can achieve when combined with the UDF GO and GOODS ERS data.

by selecting a number N_{orbits} of orbits per pointing, assuming 46 minutes/orbit exposure time, and using the WFC3 IR channel ETC. The total number of orbits for each survey were then determined by selecting the number of fields N_{fields} , a mosaic geometry per field, and multiplying the number of pointings in each mosaic by N_{orbits} (and then doubling to account for comparable coverage in a bluer WFC3 filter).

The survey models are designed to cover a large range in total area ($A_{\text{tot}} \approx 14 - 3600$ square arcmin), field numbers ($N_{\text{fields}} = 1 - 4$), orbits per pointing ($N_{\text{orbits}} = 0.5 - 125$), limiting depth ($H_{\text{AB}} \approx 27 - 30$), and total number of orbits (450 - 900). We design each survey to approximate possible HST WFC3 tilings of existing surveys; as such, these model surveys represent realistic extensions of existing HST and Spitzer surveys to hundreds of orbits of WFC3 coverage. Summaries of the model surveys can be found in Table 3, and are ordered by decreasing limiting depth and increasing total area. Brief descriptions of the models follow:

TABLE 3
MODEL SURVEYS

Model Name	Field Mosaic [# Point. \times # Point.]	Field Geometry [Arcmin. \times Arcmin.]	N_{fields} [#]	Total Area [Sq. Arcmin.]	$N_{\text{orbits}}^{\text{a}}$ [#]	H -band Depth [AB Mag.]	Total Orbits ^b [#]
Survey A	1×1	$2.05' \times 2.27'$	3	13.96	125	30.12	750
Survey B1	5×7	$10.3' \times 15.9'$	2	325.7	8	28.62	896
Survey B2	5×7	$10.3' \times 15.9'$	2	325.7	6	28.46	672
Survey B3	5×7	$10.3' \times 15.9'$	2	325.7	4	28.23	448
Survey C	4×13	$8.2' \times 29.5'$	4	967.6	2	27.84	832
Survey D	26×30	$59.0' \times 61.5'$	1	3628.5	0.5	27.00	780

^a Number of orbits per pointing.

^b We assume each survey will require comparable coverage in two WFC3 filters, which doubles the required number of total orbits.

using $N_{\text{fields}} > 1$ results in a substantial reduction of sample variance (see Figure 1). The model Survey A will therefore use $N_{\text{fields}} = 3$, $N_{\text{orbits}} = 125$, and $A_{\text{tot}} = 13.96$ square arcmin (three WFC3 pointings), and 750 total orbits including coverage in a bluer WFC3 filter. For calculating constraints from a combination of Survey A with existing data, we assume the Survey A fields will be able to leverage the GOODS ERS data but will duplicate the UDF GO data¹⁰.

6.2. Survey B1

Another template for a model survey is deep WFC3 coverage of the GOODS survey fields. A 5×7 WFC3 mosaic could cover a field of size $10.3' \times 15.9'$, similar to the GOODS fields (Giavalisco et al. 2004). Covering $N_{\text{fields}} = 2$ fields the size of the GOODS fields would require 70 pointings, and would cover a total area of $A_{\text{tot}} = 326$ square arcmin. Using $N_{\text{orbits}} = 8$ orbits per pointing would reach $H_{\text{AB}} = 28.6$ in F140W, and would require a total of 896 orbits (including coverage in a bluer WFC3 filter). Survey B1 is the most expensive survey we consider. For calculating combined constraints utilizing existing, we will combine Survey B1 with the UDF GO data but ignore the duplicated GOODS ERS F160W data¹¹.

6.3. Survey B2

To gain intuition about the relative value of depth and area for constraining high-redshift galaxy populations, we will consider variations of the GOODS-like survey. Survey B2 is identical to Survey B1 in number of fields and pointings, but would achieve a reduced depth of $N_{\text{orbits}} = 6$ orbits per pointing ($H_{\text{AB}} = 28.46$). The total number of orbits required for Survey B2 is 672 (including equal coverage in a bluer WFC3 filter). When determining combined constraints with existing data, we will combine Survey B2 with the UDF GO survey.

6.4. Survey B3

Same as Survey B1 and Survey B2, but to $N_{\text{orbits}} = 4$ orbits per pointing ($H_{\text{AB}} = 28.2$) depth. Survey B3 would require 448 total orbits. For combined constraints with existing data, we will combine Survey B3 with UDF GO

An existing survey with a combination of large area and infrared depth is the Spitzer Extended Deep Survey (SEDS; Fazio et al. 2008), which was designed to cover 0.9 deg^2 over five fields to 12 hour/pointing depth with the warm Spitzer Infrared Array Camera $3.6 \mu\text{m}$ and $4.5 \mu\text{m}$ channels. Exactly reproducing the SEDS survey with WFC3 would likely be prohibitively expensive, so we will instead consider a feasible WFC3 survey with a design similar in spirit to SEDS. Our SEDS-like Survey C will consist of $N_{\text{fields}} = 4$ fields of 4×13 pointing mosaics (each of size $8.2' \times 29.5'$), for a total area $A_{\text{tot}} = 967.6$ square arcmin. A depth of $N_{\text{orbits}} = 2$ orbits per pointing ($H_{\text{AB}} = 27.8$) would then require 832 orbits (including equal coverage in a bluer WFC3 filter). For calculating combined constraints with existing data, we will combine Survey C with both the UDF GO and GOODS ERS fields.

6.6. Survey D

The largest HST survey to date is the equatorial Cosmic Origins Survey (COSMOS Scoville et al. 2007b), which covers 2 deg^2 with the ACS I -band. As with the SEDS-like Survey C, exactly reproducing the COSMOS survey with WFC3 would likely be prohibitively expensive. Instead, we consider a 1 deg^2 ($A_{\text{tot}} = 3629$ square arcmin) survey with a single 26×30 mosaic ($59.0' \times 61.5'$) to $N_{\text{orbits}} = 0.5$ orbits per pointing ($H_{\text{AB}} = 27$) depth. Survey D is the widest and shallowest design we consider, and would require 780 orbits to complete (including equal coverage in a bluer WFC3 filter). We will combine Survey D with both the UDF GO and GOODS ERS surveys for purposes of calculating combined constraints incorporating existing data.

6.7. Field Size Comparison

We show an illustrative comparison of the existing and model survey areas in Figure 3. The UDF GO, GOODS ERS, and Surveys A, B1, B2, B3, C, and D areas are shown as white boxes overlaid on a thin $10h^{-1}\text{Mpc}$ slice through a ΛCDM cosmological simulation of comoving size $L = 250h^{-1}\text{Mpc}$ at $z \sim 7$ (Tinker et al. 2008). The blue scale image shows the

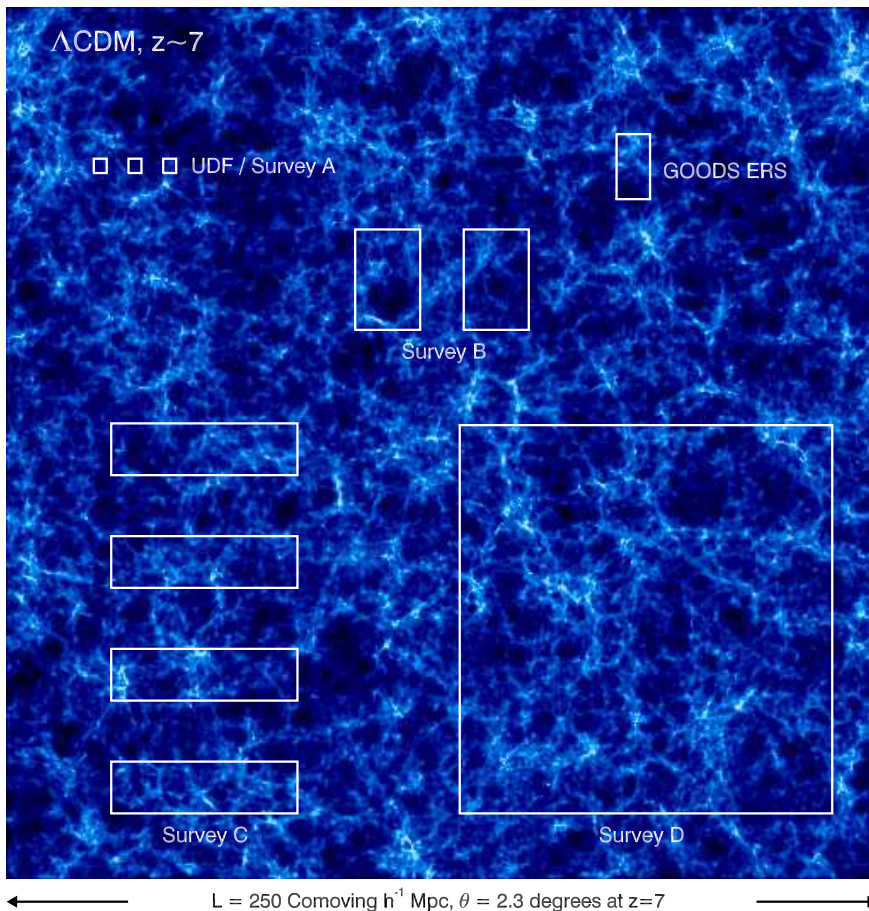


FIG. 3.— Existing and model survey areas compared with the large scale dark matter structure at $z \sim 7$. Shown are the UDF GO, GOODS ERS, Surveys A, B1, B2, B3, C, and D areas (white boxes), projected onto a surface density map of a thin $10h^{-1}\text{Mpc}$ slice through a ΛCDM cosmological simulation of size $L = 250h^{-1}\text{Mpc}$ (Tinker et al. 2008). The number of fields and survey areas of UDF GO and Survey A are identical. This comparison illustrates the characteristic angular size of large scale structures at $z \sim 7$, as well as the survey areas required to probe representative samples of the high-redshift dark matter density distribution. The separation between fields is not to scale, and model surveys incorporating different fields would likely be more widely spaced to probe statistically independent regions on the sky.

7. FORECASTED CONSTRAINTS FOR MODEL SURVEYS

The forecasted constraints calculated for the model Surveys A, B1, B2, B3, C, and D are summarized in Table 5 and presented in Figures 4-9. In each figure, the shaded areas show the projected constraints for each model survey in the $M_* - \phi_*$ (left panel), $M_* - \alpha$ (middle panel), and $\phi_* - \alpha$ (right panel) LF parameter planes. The axes ranges in Figures 4-9 are identical (and much smaller than in Figure 2), and the plotted constraints are directly comparable. A description of the forecasted constraints for each model survey follows:

7.1. Survey A

Figure 4 shows the forecasted constraints for Sur-

veys C and D. Survey A is the deepest model survey we consider, and results in the tightest forecasted constraints on the LF faint-end slope ($\Delta\alpha \approx 0.1$, marginalized). GOODS ERS complements Survey A by providing an improved combined constraint on the LF normalization ($\Delta\phi_* \approx 0.15$) and characteristic magnitude ($\Delta M_* \approx 0.22$). The combined Survey A and the GOODS ERS survey also produce relatively low correlation coefficients ($\rho \approx 0.6 - 0.85$) compared with other surveys combinations; the orientation of the $M_* - \alpha$ joint constraint from Survey A is only slightly inclined ($\Theta = 12$ deg), and allows the GOODS ERS survey ($\Theta = 55$ deg) to improve the combined constraints on M_* .

cal galaxy bias ($\langle b \rangle \approx 6.5$) and cosmic variance uncertainty ($\sigma_{\text{CV}} \approx 0.142$) in Survey B1 would be smaller than for either Survey B2 ($\langle b \rangle \approx 6.7$, $\sigma_{\text{CV}} \approx 0.146$) or Survey B3 ($\langle b \rangle \approx 7.0$, $\sigma_{\text{CV}} \approx 0.152$). Similarly, the extra depth affords more observed galaxies ($N \approx 1100$) and less Poisson uncertainty (3% fractionally) for Survey B1 than for Survey B2 ($N \approx 850$, 3.4%) or Survey B3 ($N \approx 610$, 4.1%).

The Fisher matrix calculations translate the Poisson and cosmic variance uncertainties into constraints on the LF parameters, and Figures 5-7 show how the parameter constraints scale with limiting magnitude for Surveys B1, B2, and B3. In each figure, the shaded areas show the constraints achieved by UDF GO (light blue), the model surveys (blue), and the combination of UDF GO and each model survey (dark blue). The LF parameter constraints are also listed in Table 5.

Of these three surveys, Survey B1 achieves the best combined parameters constraints ($\Delta M_* = 0.21$, $\Delta \log_{10} \phi_* = 0.176$, $\Delta \alpha = 0.172$). However, the relative gain over Survey B2 ($\Delta M_* = 0.24$, $\Delta \log_{10} \phi_* = 0.19$, $\Delta \alpha = 0.21$) and Survey B3 ($\Delta M_* = 0.25$, $\Delta \log_{10} \phi_* = 0.21$, $\Delta \alpha = 0.25$) are relatively modest (20% improvement in ΔM_* and $\Delta \log_{10} \phi_*$, and 40% in $\Delta \alpha$). Most of the relative improvement owes to the increased constraint on the LF faint-end slope for Survey B1, since the three surveys are essentially identical for galaxies with $H_{\text{AB}} < 28.2$, have a similar orientation of their error ellipse in the M_* - ϕ_* projections ($\Theta \approx 39$ deg), and have similar correlations between LF parameters. Combining with UDF GO results in a larger relative improvement in the LF parameter constraints for Survey B2 (10%) and Survey B3 (20-25%) than for Survey B1 (5%).

7.3. Survey C

The next widest model survey design is Survey C, with a total area of $A_{\text{tot}} = 967.6$ square arcmin to $H_{\text{AB}} = 27.8$ depth over $N_{\text{fields}} = 4$ fields. Such a survey would find $N \approx 940$ galaxies at $z \sim 7$, with an average bias of $\langle b \rangle = 7.5$, cosmic variance uncertainty of $\sigma_{\text{CV}} \approx 0.1$, and Poisson uncertainty of 3%.

Figure 8 shows the constraints for Survey C (blue region), the combination of UDF GO and GOODS ERS (light blue region), and the combination of all three surveys (dark blue region). The larger area of Survey C allows for better or comparable combined constraints on the LF characteristic magnitude ($\Delta M_* \approx 0.19$) and normalization ($\Delta \log_{10} \phi_* \approx 0.15$) than deeper surveys over smaller areas. Owing to its weaker constraint on the faint-end slope, the error ellipses provided by Survey C are more highly inclined in the M_* - α ($\Theta \approx 50$ deg) and ϕ_* - α ($\Theta \approx 59$ deg) projections than the UDF GO-GOODS ERS combined constraints (38 and 44 deg). When combined with UDF GO and GOODS ERS surveys, Survey C would provide among the tightest constraints of the surveys we consider (with Survey A providing better combined constraints on α and Survey D providing better constraints on M_* , ϕ_* , and α).

the Poisson errors of individual magnitude bins on the bright end of the LF, and the Poisson error is independent of N_{fields} for surveys of fixed total area. For magnitude bins that are Poisson-uncertainty dominated, the improvement in the cosmic sample variance gained by increasing N_{fields} therefore may not strongly influence end constraints on the LF parameters.

7.4. Survey D

The widest and shallowest model survey design considered is the single-field Survey D ($A_{\text{tot}} \approx 1 \text{ deg}^2$, $H_{\text{AB}} = 27$, $N_{\text{fields}} = 1$). This model survey would find $N \approx 570$ galaxies at $z \sim 7$, probing only galaxies brighter than M_* with an average bias of $\langle b \rangle \approx 9$ with a cosmic variance uncertainty of $\sigma_{\text{CV}} \approx 0.11$ (dominating over the Poisson uncertainty of 4.2%). Figure 9 shows the constraints that would be achieved by the combination of UDF GO and GOODS ERS (light blue region), Survey D individually (blue region), and the combination of all three surveys (dark blue region).

The constraints achievable by Survey D individually are comparable to the constraints provided by combining UDF GO and GOODS ERS, but would require roughly three times as much additional telescope time to complete. However, the combination of Survey D with both UDF GO and GOODS ERS produces the strongest joint constraint of any survey design we considered ($\Delta M_* \approx 0.136$, $\Delta \log_{10} \phi_* \approx 0.11$, $\Delta \alpha \approx 0.20$). The orientation of constraint provided by Survey D individually is inclined ($\Theta = [29.5, 65.4, 76.2]$) relative to the UDF GO-GOODS ERS combination ($\Theta = [38.9, 37.6, 44.3]$), and results in a relatively low correlation between the LF normalization and faint-end slope ($\rho \approx 0.77$). While other survey designs produce better constraints on the faint-end slope, the joint constraint region shown in Figure 9 produces an uncertainty in the LF that is better than $\approx 6\%$ at all relatively bright ($H_{\text{AB}} \lesssim 28$) magnitudes.

8. DISCUSSION

We have considered the problem of forecasting constraints on parameters of the $z \sim 7$ LF given the characteristics of ongoing surveys and models for potential future survey designs. The purview of our calculation was purposefully narrow since a more comprehensive evaluation of galaxy surveys could involve many additional questions we have not addressed. We now turn to a variety of possible caveats that stem from considering photometric galaxy survey designs more generally.

We have focused on forecasting constraints for the luminosity function. Our approach was modeled after Fisher matrix calculations that used the abundance of galaxy clusters to forecast cosmological parameters constraints (Hu & Kravtsov 2003; Lima & Hu 2004, 2005; Cunha & Evrard 2009; Wu et al. 2009), but other previous calculations have forecasted cosmological parameter constraints from galaxy clustering (e.g., Vogeley & Szalay 1996; Matsubara & Szalay 2001, 2003; Linder 2003; Albrecht et al.

the combination of existing deep/narrow surveys with a future wide/shallow survey or a future ultradeep/narrow survey would provide tight constraints on the $z \sim 7$ luminosity function, studies of the galaxy population at higher and lower redshifts could require substantially different surveys. For instance, the $z \gtrsim 8$ dropout candidates identified in the UDF GO data are all fainter than $H_{AB} = 27.7$ (Bouwens et al. 2009a; Bunker et al. 2009; McLure et al. 2009; Yan et al. 2009). The decreasing abundance of relatively bright galaxies with increasing redshift will tend to favor deeper and narrow surveys. Our calculations can easily be extended to estimate the constraining power of various surveys designs for higher-redshift galaxy populations, but we will save such estimates for future work when better fiducial estimates of the $z \gtrsim 8$ luminosity function are available.

Our Fisher matrix approach requires the use of a fiducial model for the abundance of $z \sim 7$. We adopt the Oesch et al. (2010b) estimate of the galaxy luminosity function, which was determined by scaling the characteristic magnitude M_* and normalization ϕ_* from lower redshift data and then fitting for the faint-end slope α . If the $z \sim 7$ galaxy luminosity function differs substantially from the Oesch et al. (2010b) estimate, then our forecasted constraints could be similarly inaccurate. For instance, if the normalization ϕ_* was considerably lower or the characteristic magnitude M_* much fainter than that estimate by Oesch et al. (2010b), then the relative benefit of combining the UDF GO and GOODS ERS data with a wide/shallow survey over a narrow/ultradeep design could be reduced.

The calculations in §2.4.1 and §7 suggest that splitting wide surveys into multiple fields to probe statistically-independent regions of the universe may not dramatically improve constraints on the galaxy luminosity function. While this conclusion depends strongly on the total volume of the survey, other considerations such as scheduling, field observability, or sky backgrounds could make multiple fields advantageous compared with a single contiguous field of the same total area.

The abundance matching calculation also requires either knowledge or assumption about the completeness of the survey and the fraction of dark matter halos occupied by galaxies. We have assumed that the surveys are essentially volume-limited and that there is a one-to-one correspondence between galaxies and dark matter halos. Both of these assumptions are likely imperfect, and some estimates of the high-redshift occupation fraction are as low as 20% (Stark et al. 2007b). The influence of these assumptions over the forecasted parameter constraints depends on the character of the survey. For a given observed luminosity function, reducing the halo occupation fraction or the survey completeness acts to reduce the effective galaxy bias in the survey by either increasing the number of halos per galaxy in the survey or increasing the number of undetected galaxies. In either case, the Poisson uncertainty is based on the observed number of galaxies

9. SUMMARY

Motivated by the exciting initial galaxy survey data obtained by newly-installed Wide Field Camera 3 (WFC3) on the Hubble Space Telescope (HST), we have attempted to quantify how well on-going and possible future infrared surveys with WFC3 will constrain the abundance of galaxies at $z \sim 7$. Our primary methods and results include:

- We perform a Fisher matrix calculation to forecast constraints on the galaxy luminosity function (LF) achievable by a survey with a given depth, area, and number of fields. In our approach, the constraints on the LF normalization ϕ_* , characteristic magnitude M_* , and faint-end slope α that a survey can achieve directly relate to the sample cosmic variance and Poisson uncertainty on the observed galaxy abundance through the Fisher matrix. For a fiducial LF model, the abundance of observed galaxies and dark matter halos are matched (e.g., Conroy et al. 2006; Conroy & Wechsler 2009) to estimate the bias of galaxies of a given luminosity. The galaxy bias is combined with the RMS density fluctuations within the survey volume to calculate the sample cosmic variance (e.g., Newman & Davis 2002; Somerville et al. 2004; Stark et al. 2007b; Trenti & Stiavelli 2008), while the Poisson variance simply scales with the square root of the number of observed galaxies. The constraining power of each survey is then calculated from the Fisher matrix using the Schechter (1976) model of the LF, its derivatives, the sample cosmic variance and Poisson uncertainties, and any data covariance. The combined constraints from multiple surveys can be estimated easily by summing their Fisher matrices. Similar calculations should prove useful for designing future photometric surveys and estimating their constraining power for the galaxy LF.
- Using the Fisher matrix calculations, we estimate the constraints on the abundance of $z \sim 7$ galaxies that will be achieved with the entire forthcoming Ultradeep Field Guest Observation (UDF GO) and Great Observatories Origins Deep Survey Early-Release Science (GOODS ERS) HST WFC3 IR channel data. Using the $z \sim 7$ galaxy LF estimated by Oesch et al. (2010b) as a fiducial model, we calculate that the combined UDF GO and GOODS ERS data will achieve marginalized (unmarginalized) LF parameter constraints of $\Delta M_* \approx 0.5$ mag (0.1 mag), $\Delta \log_{10} \phi_* \approx 0.4$ (0.1), and $\Delta \alpha \approx 0.4$ (0.15) when the surveys are fully completed. These marginalized constraints correspond to uncertainties in the total number of $z \sim 7$ galaxies with magnitudes $M_{UV} < -18$ ($M_{UV} < M_* \approx -19.8$) of 25% (200%), after accounting for covariances between the

abundance of $z \sim 7$ galaxies. When combined with the forthcoming UDF GO and GOODS ERS data, all the surveys considered produce interesting luminosity function constraints (see Table 5). We find that a $\sim 1 \text{ deg}^2$ survey to $H_{AB} \approx 27$ in F140W provides the tightest combined marginalized constraints ($\Delta M_* \approx 0.14$, $\Delta \phi_* \approx 0.11$, $\Delta \alpha \approx 0.20$) on the abundance of $z \sim 7$ galaxies of all survey designs we consider, but only by a small margin. This survey would require 780 total orbits, including equal coverage in a bluer WFC3 filter to define a drop out color selection. In contrast, the abundance of *faint* galaxies would be best constrained by increasing depth of the HST ultradeep fields to ~ 125 orbits per pointing ($H_{AB} \approx 30.1$ in F140W), which provides marginalized LF constraints of $\Delta M_* \approx 0.22$, $\Delta \phi_* \approx 0.15$, and $\Delta \alpha \approx 0.10$ for 750 total orbits (including equal coverage in a bluer WFC3 filter).

- We also consider the usefulness of splitting surveys into N_{fields} multiple fields to probe independent samples and reduce cosmic variance uncertainties (e.g., Newman & Davis 2002). We show that the shape of the Λ CDM power spectrum limits the statistical gain of splitting a high-redshift survey into multiple fields to $\lesssim 10\%$ (for $N_{\text{fields}} = 2$) when the survey area is large ($\gtrsim 0.5 \text{ deg}^2$). We suggest that this statistical gain should be weighed against any scientific gains achieved by probing large contiguous areas.

Initial analyses of the UDF GO data have already demonstrated that the installation of WFC3 on HST will transform our knowledge of high-redshift galaxy populations at $z \sim 7$ and beyond (e.g., Bouwens et al. 2009a,b, 2010; Oesch et al. 2010b,a; Bunker et al. 2009; McLure et al. 2009; Yan et al. 2009; Wilkins et al. 2009; Labbé et al. 2009, 2010; Finkelstein et al. 2009). Our work has attempted to quantify expectations for the constraining power of the UDF GO and GOODS ERS surveys, and forecast constraints achievable with more extensive future surveys using WFC3 or other instruments. These calculations illustrate how truly powerful the refurbished HST is for exploring high-redshift galaxy populations, and emphasize how exciting near-term gains in our knowledge of $z \gtrsim 7$ galaxies will be.

I thank Peter Capak and Nick Scoville for useful advice on modeling the survey data and WFC3 observations, Richard Ellis for helpful discussions, and Anatoly Klypin for permission to use his cosmological simulation. I am supported by a Hubble Fellowship grant, program number HST-HF-51262.01-A provided by NASA from the Space Telescope Science Institute, which is operated by the Association of Universities for Research in Astronomy, Incorporated, under NASA contract NAS5-26555. I also thank the Caltech Astronomy Department for hosting me during my Hubble Fellowship.

REFERENCES

- Albrecht, A., et al. 2009, ArXiv e-prints
 Barton, E. J., Davé, R., Smith, J., Papovich, C., Hernquist, L., & Springel, V. 2004, ApJ, 604, L1
 Behroozi, P. S., Conroy, C., & Wechsler, R. H. 2010, ArXiv e-prints
 Bond, J. R., & Myers, S. T. 1996, ApJS, 103, 1
 Bouwens, R. J., et al. 2009a, ApJ, 690, 1764
 Bouwens, R. J., Illingworth, G. D., Franx, M., & Ford, H. 2008, ApJ, 686, 230
 Bouwens, R. J., et al. 2009b, ArXiv e-prints
 —. 2010, ApJ, 708, L69
 Bouwens, R. J., Illingworth, G. D., Thompson, R. I., & Franx, M. 2005, ApJ, 624, L5
 Bouwens, R. J., et al. 2004, ApJ, 616, L79
 Bradley, L. D., et al. 2008, ApJ, 678, 647
 Bunker, A., et al. 2009, ArXiv e-prints
 Castellano, M., et al. 2009, ArXiv e-prints
 Conroy, C., & Wechsler, R. H. 2009, ApJ, 696, 620
 Conroy, C., Wechsler, R. H., & Kravtsov, A. V. 2006, ApJ, 647, 201
 Crocce, M., Pueblas, S., & Scoccimarro, R. 2006, MNRAS, 373, 369
 Cuby, J., Hibon, P., Lidman, C., Le Fèvre, O., Gilmozzi, R., Moorwood, A., & van der Werf, P. 2007, A&A, 461, 911
 Cunha, C. E., & Evrard, A. E. 2009, ArXiv e-prints
 Davé, R., Finlator, K., & Oppenheimer, B. D. 2006, MNRAS, 370, 273
 Dayal, P., Ferrara, A., Saro, A., Salvaterra, R., Borgani, S., & Tornatore, L. 2009, MNRAS, 400, 2000
 Dayal, P., Ferrara, A., & Saro, A. 2009, to appear in MNRAS
 Egami, E., et al. 2005, ApJ, 618, L5
 Gunn, J. E., & Gott, J. R. I. 1972, ApJ, 176, 1
 Haiman, Z. 2002, ApJ, 576, L1
 Hansen, M., & Oh, S. P. 2006, MNRAS, 367, 979
 Henry, A. L., Malkan, M. A., Colbert, J. W., Siana, B., Teplitz, H. I., & McCarthy, P. 2008, ApJ, 680, L97
 Henry, A. L., Malkan, M. A., Colbert, J. W., Siana, B., Teplitz, H. I., McCarthy, P., & Yan, L. 2007, ApJ, 656, L1
 Henry, A. L., et al. 2009, ApJ, 697, 1128
 Hibon, P., et al. 2009, ArXiv e-prints
 Hickey, S., Bunker, A., Jarvis, M. J., Chiu, K., & Bonfield, D. 2009, ArXiv e-prints
 Holder, G., Haiman, Z., & Mohr, J. J. 2001, ApJ, 560, L111
 Hu, W., & Cohn, J. D. 2006, Phys. Rev. D, 73, 067301
 Hu, W., & Kravtsov, A. V. 2003, ApJ, 584, 702
 Iye, M., et al. 2006, Nature, 443, 186
 Kaiser, N. 1984, ApJ, 284, L9
 Kashikawa, N., et al. 2006, ApJ, 648, 7
 Kitzbichler, M. G., & White, S. D. M. 2007, MNRAS, 376, 2
 Kneib, J., Ellis, R. S., Santos, M. R., & Richard, J. 2004, ApJ, 607, 697
 Kobayashi, M. A. R., Totani, T., & Nagashima, M. 2007, ApJ, 670, 919
 —. 2010, ApJ, 708, 1119
 Kodaira, K., et al. 2003, PASJ, 55, L17
 Komatsu, E., et al. 2009, ApJS, 180, 330
 Kowalski, M., et al. 2008, ApJ, 686, 749
 Kravtsov, A. V., Berlind, A. A., Wechsler, R. H., Klypin, A. A., Gottlöber, S., Allgood, B., & Primack, J. R. 2004, ApJ, 609, 35
 Labbé, I., et al. 2009, ArXiv e-prints

- McLure, R. J., Dunlop, J. S., Cirasuolo, M., Koekemoer, A. M., Sabbi, E., Stark, D. P., Targett, T. A., & Ellis, R. S. 2009, ArXiv e-prints
- McQuinn, M., Hernquist, L., Zalzarriaga, M., & Dutta, S. 2007, MNRAS, 381, 75
- Mesinger, A., & Furlanetto, S. R. 2008, MNRAS, 386, 1990
- Mo, H. J., & White, S. D. M. 1996, MNRAS, 282, 347
- Newman, J. A., & Davis, M. 2002, ApJ, 564, 567
- Nilsson, K. K., Orsi, A., Lacey, C. G., Baugh, C. M., & Thommes, E. 2007, A&A, 474, 385
- Oesch, P. A., et al. 2010a, ApJ, 709, L21
- . 2010b, ApJ, 709, L16
- . 2009, ApJ, 690, 1350
- Oke, J. B., & Gunn, J. E. 1983, ApJ, 266, 713
- Ota, K., et al. 2008, ApJ, 677, 12
- Ouchi, M., et al. 2009a, ApJ, 706, 1136
- . 2009b, ApJ, 696, 1164
- Parkes, I. M., Collins, C. A., & Joseph, R. D. 1994, MNRAS, 266, 983
- Peacock, J. A., & Dodds, S. J. 1996, MNRAS, 280, L19
- Percival, W. J., Cole, S., Eisenstein, D. J., Nichol, R. C., Peacock, J. A., Pope, A. C., & Szalay, A. S. 2007, MNRAS, 381, 1053
- Richard, J., Pelló, R., Schaerer, D., Le Borgne, J., & Kneib, J. 2006, A&A, 456, 861
- Richard, J., Stark, D. P., Ellis, R. S., George, M. R., Egami, E., Kneib, J., & Smith, G. P. 2008, ApJ, 685, 705
- Samui, S., Srianand, R., & Subramanian, K. 2009, MNRAS, 398, 2061
- Santos, M. R. 2004, MNRAS, 349, 1137
- Santos, M. R., Ellis, R. S., Kneib, J., Richard, J., & Kuijken, K. 2004, ApJ, 606, 683
- Schechter, P. 1976, ApJ, 203, 297
- Scoville, N., et al. 2007a, ApJS, 172, 38
- . 2007b, ApJS, 172, 1
- Sheth, R. K., Mo, H. J., & Tormen, G. 2001, MNRAS, 323, 1
- Sheth, R. K., & Tormen, G. 1999, MNRAS, 308, 119
- Smith, R. E., et al. 2003, MNRAS, 341, 1311
- Sobral, D., et al. 2009, MNRAS, 398, L68
- Somerville, R. S., Lee, K., Ferguson, H. C., Gardner, J. P., Moustakas, L. A., & Giavalisco, M. 2004, ApJ, 600, L171
- Springel, V., et al. 2005, Nature, 435, 629
- Stanway, E. R., Bremer, M. N., Squitieri, V., Douglas, L. S., & Lehnert, M. D. 2008, MNRAS, 386, 370
- Stark, D. P., & Ellis, R. S. 2006, New Astronomy Review, 50, 46
- Stark, D. P., Ellis, R. S., Richard, J., Kneib, J., Smith, G. P., & Santos, M. R. 2007a, ApJ, 663, 10
- Stark, D. P., Loeb, A., & Ellis, R. S. 2007b, ApJ, 668, 627
- Taniguchi, Y., et al. 2005, PASJ, 57, 165
- Tasitsiomi, A. 2006, ApJ, 645, 792
- Tegmark, M., Taylor, A. N., & Heavens, A. F. 1997, ApJ, 480, 22
- Tilvi, V., Malhotra, S., Rhoads, J. E., Scannapieco, E., Thacker, R. J., Iliev, I. T., & Mellema, G. 2009, ApJ, 704, 724
- Tinker, J., Kravtsov, A. V., Klypin, A., Abazajian, K., Warren, M., Yepes, G., Gottlöber, S., & Holz, D. E. 2008, ApJ, 688, 709
- Tinker et al. 2010, in preparation
- Trenti, M., & Stiavelli, M. 2008, ApJ, 676, 767
- Vogeley, M. S., & Szalay, A. S. 1996, ApJ, 465, 34
- Warren, M. S., Abazajian, K., Holz, D. E., & Teodoro, L. 2006, ApJ, 646, 881
- Wilkins, S. M., Bunker, A. J., Ellis, R. S., Stark, D., Stanway, E. R., Chiu, K., Lorenzoni, S., & Jarvis, M. J. 2009, ArXiv e-prints
- Willis, J. P., & Courbin, F. 2005, MNRAS, 357, 1348
- Willis, J. P., Courbin, F., Kneib, J., & Minniti, D. 2008, MNRAS, 384, 1039
- Wu, H., Zentner, A. R., & Wechsler, R. H. 2009, ArXiv e-prints
- Wyithe, J. S. B., & Loeb, A. 2005, ApJ, 625, 1
- Yan, H., Windhorst, R., Hathi, N., Cohen, S., Ryan, R., O'Connell, R., & McCarthy, P. 2009, ArXiv e-prints
- Yepes, G., Sevilla, R., Gottlöber, S., & Silk, J. 2007, ApJ, 666, L61
- Zheng, W., et al. 2009, ApJ, 697, 1907

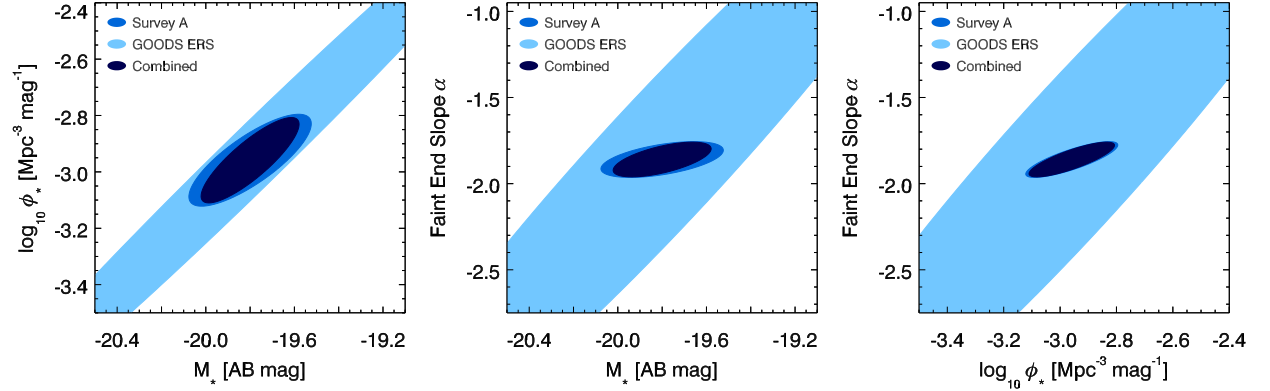


FIG. 4.— Forecasted constraints on $z \sim 7$ luminosity function parameters expected from the existing GOODS ERS survey and the model Survey A. The constraints are calculated for a Schechter (1976) luminosity function with a characteristic luminosity M_* , normalization ϕ_* , and faint-end slope α . Shown are the $1-\sigma$ constraints in the $M_* - \log_{10} \phi_*$ (left panel), $M_* - \alpha$ (middle panel), and $\log_{10} \phi_* - \alpha$ (right panel) space projections for the GOODS ERS (light blue region) and Survey A (blue region) surveys. Also shown are the constraints expected by combining both surveys (dark blue region).

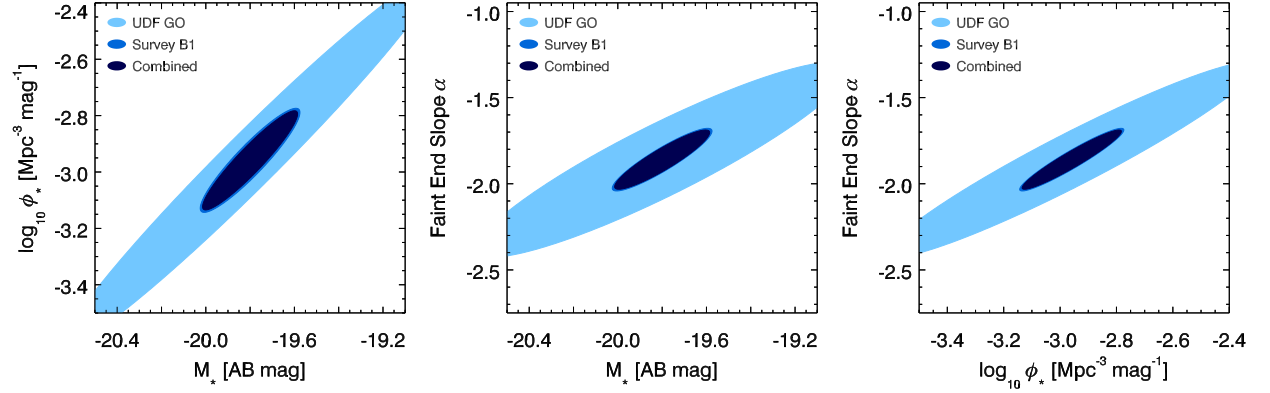
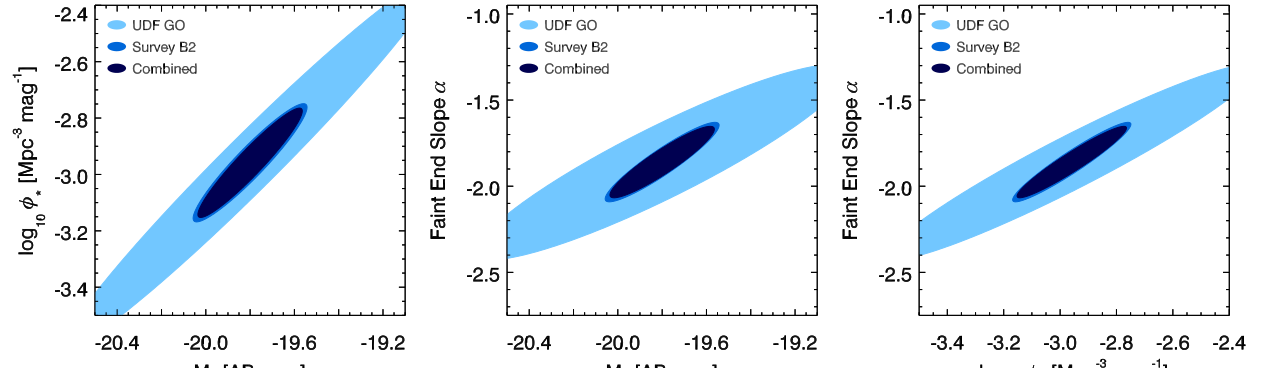


FIG. 5.— Forecasted constraints on $z \sim 7$ luminosity function parameters expected from the existing UDF GO survey and the model Survey B1. The constraints are calculated for a Schechter (1976) luminosity function with a characteristic luminosity M_* , normalization ϕ_* , and faint-end slope α . Shown are the $1-\sigma$ constraints in the $M_* - \log_{10} \phi_*$ (left panel), $M_* - \alpha$ (middle panel), and $\log_{10} \phi_* - \alpha$ (right panel) space projections for the UDF GO (light blue region) and Survey B1 (blue region) surveys. Also shown are the constraints expected by combining both surveys (dark blue region).



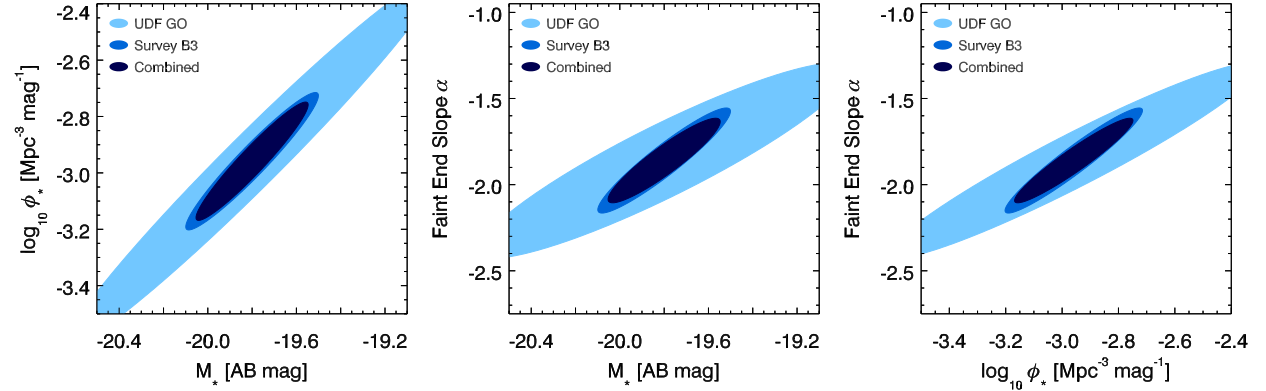


FIG. 7.— Forecasted constraints on $z \sim 7$ luminosity function parameters expected from the existing UDF GO survey and the model Survey B3. The constraints are calculated for a Schechter (1976) luminosity function with a characteristic luminosity M_* , normalization ϕ_* , and faint-end slope α . Shown are the $1-\sigma$ constraints in the $M_* - \log_{10} \phi_*$ (left panel), $M_* - \alpha$ (middle panel), and $\log_{10} \phi_* - \alpha$ (right panel) space projections for the UDF GO (light blue region) and Survey B3 (blue region) surveys. Also shown are the constraints expected by combining both surveys (dark blue region).

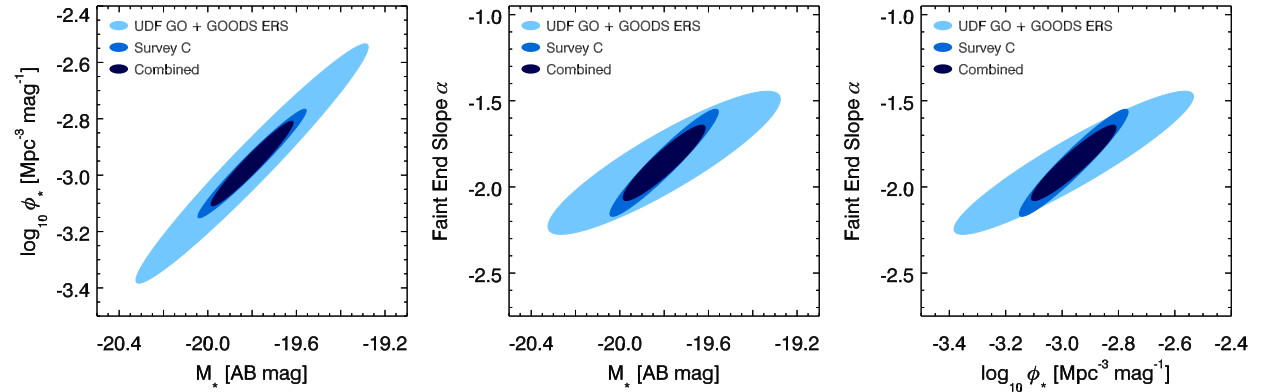


FIG. 8.— Forecasted constraints on $z \sim 7$ luminosity function parameters expected from the existing UDF GO and GOODS ERS surveys and the model Survey C. The constraints are calculated for a Schechter (1976) luminosity function with a characteristic luminosity M_* , normalization ϕ_* , and faint-end slope α . Shown are the $1-\sigma$ constraints in the $M_* - \log_{10} \phi_*$ (left panel), $M_* - \alpha$ (middle panel), and $\log_{10} \phi_* - \alpha$ (right panel) space projections for the combined UDF GO and GOODS ERS surveys (light blue region) and the model Survey C (blue region). Also shown are the constraints expected by combining all three surveys (dark blue region).

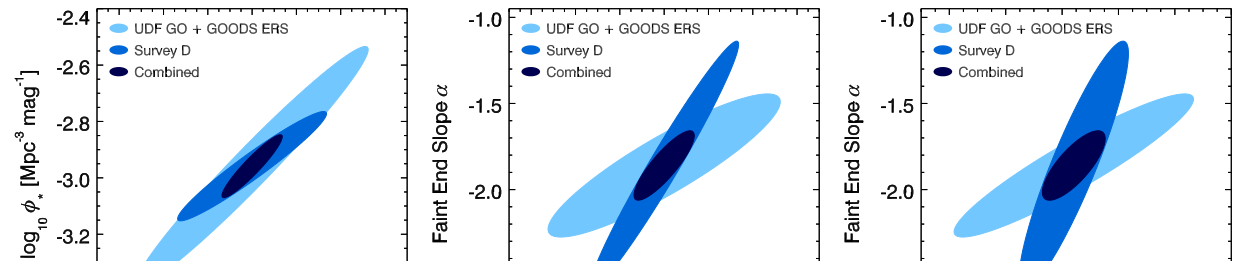


TABLE 4
FORECASTED CONSTRAINTS FOR EXISTING SURVEYS

Survey Name	Marg. Uncert. M_*	Unmarg. Uncert. M_*	Marg. Uncert. $\log_{10} \phi_*$	Unmarg. Uncert. $\log_{10} \phi_*$	Marg. Uncert. α	Unmarg. Uncert. α
UDF GO	0.837	0.160	0.655	0.093	0.566	0.162
GOODS ERS	1.338	0.171	1.026	0.145	1.852	0.520
Combined	0.524	0.117	0.425	0.078	0.415	0.154

Survey Name	Pearson ρ $M_* - \log_{10} \phi_*$	Pearson ρ $M_* - \alpha$	Pearson ρ $\log_{10} \phi_* - \alpha$	$\Theta(M_* - \phi_*)$ [deg]	$\Theta(M_* - \alpha)$ [deg]	$\Theta(\phi_* - \alpha)$ [deg]
UDF GO	0.98	0.91	0.95	38	33	41
GOODS ERS	0.99	0.96	0.95	37	55	62
Combined	0.97	0.89	0.93	39	38	44

TABLE 5
FORECASTED CONSTRAINTS FOR MODEL SURVEYS

Survey Name	Marg. Uncert. M_*	Unmarg. Uncert. M_*	Marg. Uncert. $\log_{10} \phi_*$	Unmarg. Uncert. $\log_{10} \phi_*$	Marg. Uncert. α	Unmarg. Uncert. α
Survey A	0.276	0.158	0.163	0.064	0.104	0.057
Survey B1	0.225	0.084	0.185	0.053	0.182	0.055
Survey B2	0.257	0.084	0.210	0.057	0.231	0.068
Survey B3	0.299	0.085	0.244	0.061	0.305	0.089
Survey C	0.244	0.052	0.193	0.041	0.311	0.088
Survey D	0.336	0.041	0.194	0.045	0.722	0.137
Ex.+Survey A ^a	0.221	0.116	0.151	0.058	0.101	0.057
Ex.+Survey B1 ^b	0.214	0.074	0.176	0.046	0.172	0.052
Ex.+Survey B2 ^b	0.236	0.074	0.194	0.049	0.207	0.063
Ex.+Survey B3 ^b	0.253	0.075	0.210	0.051	0.245	0.078
Ex.+Survey C ^c	0.185	0.048	0.150	0.036	0.219	0.077
Ex.+Survey D ^c	0.136	0.039	0.111	0.039	0.201	0.103

Survey Name	Pearson ρ $M_* - \log_{10} \phi_*$	Pearson ρ $M_* - \alpha$	Pearson ρ $\log_{10} \phi_* - \alpha$	$\Theta(M_* - \phi_*)$ [deg]	$\Theta(M_* - \alpha)$ [deg]	$\Theta(\phi_* - \alpha)$ [deg]
Survey A	0.79	0.52	0.81	28	12	30
Survey B1	0.92	0.91	0.95	39	38	45
Survey B2	0.94	0.93	0.95	39	42	48
Survey B3	0.95	0.94	0.95	39	46	52
Survey C	0.97	0.95	0.95	38	52	59
Survey D	0.96	0.97	0.90	29	65	76
Ex.+Survey A ^a	0.84	0.62	0.82	33	18	31
Ex.+Survey B1 ^b	0.94	0.91	0.95	39	38	44
Ex.+Survey B2 ^b	0.95	0.92	0.95	39	41	47
Ex.+Survey B3 ^b	0.95	0.92	0.95	39	44	50
Ex.+Survey C ^c	0.96	0.92	0.93	39	50	56
Ex.+Survey D ^c	0.93	0.86	0.77	39	58	65

^a Combined with the existing GOODS ERS survey.

^b Combined with the existing UDF GO survey.

^c Combined with the existing UDF GO and GOODS ERS surveys.